



Electron irradiation of nuclear graphite studied by transmission electron microscopy and electron energy loss spectroscopy

B.E. Mironov, H.M. Freeman, A.P. Brown, F.S. Hage, A.J. Scott, A.V.K. Westwood, Jean-Pierre da Costa, P. Weisbecker, R.M.D. Brydson

► To cite this version:

B.E. Mironov, H.M. Freeman, A.P. Brown, F.S. Hage, A.J. Scott, et al.. Electron irradiation of nuclear graphite studied by transmission electron microscopy and electron energy loss spectroscopy. Carbon, 2015, 83, pp.12. 10.1016/j.carbon.2014.11.019 . hal-01120154

HAL Id: hal-01120154

<https://hal.science/hal-01120154>

Submitted on 25 Feb 2015

HAL is a multi-disciplinary open access archive for the deposit and dissemination of scientific research documents, whether they are published or not. The documents may come from teaching and research institutions in France or abroad, or from public or private research centers.

L'archive ouverte pluridisciplinaire **HAL**, est destinée au dépôt et à la diffusion de documents scientifiques de niveau recherche, publiés ou non, émanant des établissements d'enseignement et de recherche français ou étrangers, des laboratoires publics ou privés.

Electron irradiation of nuclear graphite studied by transmission electron microscopy and electron energy loss spectroscopy

B. E. Mironov^{1,}, H. M. Freeman^{1,*}, A. P. Brown¹, F. S. Hage², A. J. Scott¹, A. V. K. Westwood¹, J. -P. Da Costa³, P. Weisbecker⁴, R. M. D. Brydson^{1,2},*

¹ *Institute for Materials Research, Univ. Leeds, Leeds, UK, LS2 9JT*

² *SuperSTEM, STFC Daresbury Laboratories, Daresbury, UK, WA4 4AD*

³ *Univ. Bordeaux, BSA, Laboratoire de l'Intégration du Matériau au Système, UMR 5218 CNRS-IPB – Université de Bordeaux, 33405 Talence, France*

⁴ *CNRS, Laboratoire des Composites Thermo Structuraux, UMR 5801 CNRS- Herakles- CEA - Université de Bordeaux, 33600 Pessac, France*

Abstract

Structural and chemical bonding changes in nuclear graphite have been investigated during in-situ electron irradiation in a transmission electron microscope (TEM); electron beam irradiation has been employed as a surrogate for neutron irradiation of nuclear grade graphite in nuclear reactors. This paper aims to set out a methodology for analysing the microstructure of electron-irradiated graphite which can then be extended to the analysis of neutron-irradiated graphites. The damage produced by exposure to 200 keV electrons was examined up to a total dose of approximately 0.5 dpa (equivalent to an electron fluence of 5.6×10^{21} electrons cm^{-2}). During electron exposure, high resolution TEM images (HRTEM) and electron energy loss spectra (EELS) were acquired periodically in order to record changes in structural (dis)order and chemical bonding, by quantitatively analysing the variation in phase contrast images and EEL spectra.

1 Introduction

Over 80% of the UK's current nuclear reactors are graphite-moderated Advanced Gas Cooled Reactors (AGR) or Magnox reactors [1]. In addition to moderating the energies of neutrons in the fission process, the graphite core provides structural support, contains the fuel and control rods and allows for coolant flow. The graphite blocks are subject to high levels of neutron irradiation resulting in chemical and physical property changes, which in turn affect neighbouring reactor components. The lifetime of such reactors is therefore primarily limited

* Corresponding authors: Tel: +441133432366. E-mail bemironov@gmail.com (B. E. Mironov); Tel: +441133432391. E-mail: helenfreeman88@gmail.com (H. M. Freeman)

by the performance of the irreplaceable graphite within the working reactor, so an accurate measure of its condition is essential for economic success and plant safety.

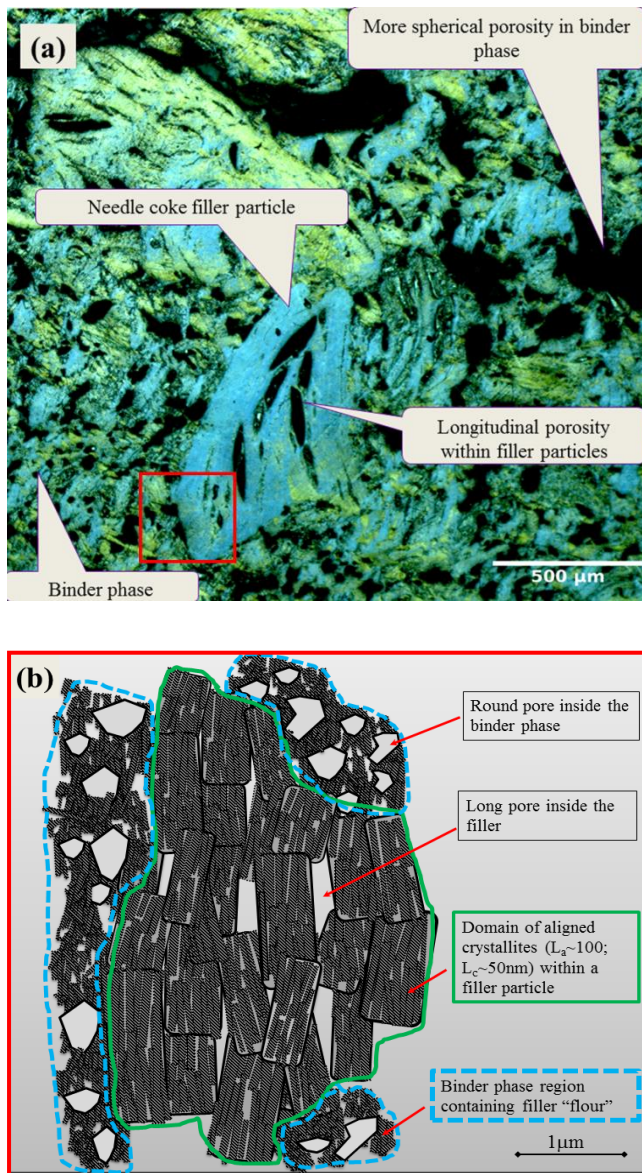


Figure 1 (a) Polarised light micrograph of pile grade A (PGA) nuclear graphite showing the main constitutive elements, with the outlined area in red corresponding to (b), a schematic of short range features within the filler particle (outlined in green) and binder phase (outlined in blue).

Nuclear graphite is a synthetic material produced from pitch and petroleum coke particles, with a high degree of crystallinity following thermal treatment at high temperatures (graphitization) [2]. When the graphitization process is complete, two main features can be distinguished: the majority filler particles and a minority binder phase, both of which are formed by domains of aligned individual crystallites and appear as a single colour in a polarised light micrograph. Both features have potentially inter- and intra- structural porosity

ranging from Mrozowski cracks between crystallites (50 nm -10 μ m) to micro- and macropores around domains and particles (Figure 1) [3].

For over 70 years, a considerable body of evidence has been assembled to understand the behaviour of irradiated graphite [2,4–6]. The bulk properties of damage features have been thoroughly investigated and theoretical models of induced structural changes derived [7]. Although this has allowed property changes in the irradiated bulk to be partly understood and accounted for in current and future graphite based reactor designs, the mechanisms of such processes at the nanoscale still remain uncertain. This work investigates the effect of electron irradiation on nuclear grade graphites within a transmission electron microscope (TEM) in an attempt to understand the fundamental processes involved in radiation damage.

1.1 Irradiation of nuclear graphite

Throughout this paper we will compare the effects of neutron and electron irradiation therefore it is important to understand the key differences between the two. The atomic displacement rate of the carbon atoms in the graphite is measured in displacements per atom (dpa) and is dependent on the kinetic energy of the incident particle [2]. According to calculations by Thrower and Mayer [8] a 1 MeV electron and neutron produce an average of 1.6 and 500 atomic displacements respectively. It is generally understood that cascades of atomic displacements are the most common route for large scale structural disturbances and models have been developed to calculate the number of atoms involved in cascade events resulting from different incident energies [9].

When mimicking the effects of neutron irradiation damage with electron irradiation in the TEM, it is important to account for both the higher dose rate of electrons compared to neutrons in a nuclear reactor (greater by about 10^4) and the reduced displacements per atom from electrons due to the lower mass [10]. Electron irradiation causes point defect damage whereas the higher mass and lower dose rate of neutrons causes cascade damage. However, the relatively wide spacing of graphite's basal planes results in a low density of the cascade events, and the low neutron dose rates (10^{-7} dpa s^{-1}) and high temperatures (~ 450 °C) in the nuclear reactor allow damage to partially anneal out between cascade events [11–13]. Interstitial and vacancy defects created during irradiation can behave independently or coalesce into clusters and gradually deform the crystal lattice ultimately resulting in both chemical and physical changes. Damage accumulation at temperatures below 200 °C increases the Wigner energy and heat content of the graphite, due to a lack of atomic diffusion [14]. It is widely agreed that single vacancies become mobile at 100 – 200 °C

whereas interstitial atoms become mobile at temperatures of 500 °C [15]. Thus only at higher temperatures such as those in the Gen IV graphite moderated Very High Temperature Gas Reactors (> 300 °C) does stored energy dissipation occur by diffusion driven atomic re-ordering and the problem is addressed in the short term. Longer term exposure to a high temperature environment (> 400 °C) however, gives rise to creep and dimensional change [16–18].

The key observed changes in nuclear grade graphite as a result of neutron irradiation are micro-crack closure resulting from expansion in the *c*-direction and dimensional change from irradiation induced creep, both of which depend on the overall level of initial crystallinity [14,19]. Dimensional change is determined in a number of ways, such as directly measuring specimens before and after irradiation, using X-ray diffraction to assess crystallite behaviour, and measuring changes in cracks and porosity with electron and light microscopy and small-angle neutron scattering [16,17,20]. The fundamental dimensional changes are known to involve crystallographic expansion in the *c*-direction and contraction in the *a*-direction [3]. Initially, the expansion is largely accommodated for in cracks and pores created during the manufacturing process; Mrozowski cracks arise from the anisotropy in graphite thermal expansion coefficients and lie perpendicular to the *c*-direction hence the initial accommodation of expansion, so that the initial macroscopic response is a net shrinkage in the *a*-direction [21]. Upon further irradiation and once the cracks and pores are fully closed, irreversible net macroscopic expansion occurs. The transition between contraction and expansion is referred to as ‘turnaround’ [22,23].

Transmission electron microscopy is an established tool for characterising both electron and neutron irradiated graphite [13,24]. There are however, very few detailed TEM-EELS studies on nuclear graphites but a significant volume of work on graphitizing and non-graphitizing carbons [25,26]. In this work we will focus on quantitative analysis of atomic lattice imaging and EEL spectroscopy to elucidate the nanoscale changes that occur in irradiated graphite.

2 Experimental Details

2.1 Sample preparation

Virgin Pile Grade A (PGA) graphite sourced from the University of Manchester was chosen for inspection. PGA is a medium to coarse grain anisotropic nuclear graphite of typical density 1.74 g cm⁻³. The anisotropy of this particular graphite comes from the

tendency of the needle-like grain particles in the filler to align in the extrusion direction during the manufacturing process. Samples were crushed using an agate pestle and mortar and mixed with acetone before being dispersed onto a holey carbon-coated copper TEM grid (3mm diameter; Agar Scientific Ltd). The analysed areas had a thickness less than 0.3 times the mean free path for inelastic scattering (Λ).

2.2 *Microscope conditions*

TEM investigations were performed on an FEI CM200 field emission TEM operated at 197 kV with a tip extraction bias of 3.21 kV routinely providing an electron flux of approximately 4.24×10^{18} electrons $\text{cm}^{-2} \text{s}^{-1}$ and an EELS energy resolution of 0.7–0.8 eV, measured as the full width at half-maximum (FWHM) of the ZLP. For EELS, the microscope was operated in diffraction mode with the smallest selected area aperture inserted, giving a circular projection of approximate diameter 150 nm, a collection semi-angle of 1.6 mrad and a convergence semi-angle of approximately 0.8 mrad, (corresponding to the magic or orientation independent angle [27]). Digital images and energy loss spectra were captured using a Gatan Imaging Filter (GIF) 200 with a 1 megapixel slow scan CCD array. Data from the array (i.e. images and spectra) were processed using Gatan's Digital Micrograph software.

Unless stated otherwise, all experiments were performed at room temperature where the localised heating effect from the electron beam was considered to be negligible due to the high thermal conductivity of graphite [28]. In-situ electron irradiation damage at higher temperatures was investigated using a Gatan TEM heating holder.

2.3 *Determination of dose*

Throughout this paper we will refer to electron and neutron irradiation in three ways: fluence refers to the number of electrons or neutrons that intersect a unit area; flux is the fluence rate; and dose is the energy transferred at a given fluence. The dose, D (in dpa), is calculated using Equation 2.1 where J is the electron fluence and σ_d is the displacement cross section.

$$D = J \times \sigma_d \quad \text{Equation 2.1}$$

The displacement cross section varies with electron energy and displacement threshold energy. Referring to figure 18 from Oen (1965) [29] we measure a displacement cross section value of 16.25 barns for an electron energy of 200 keV and a displacement threshold energy

of 20 eV [30]. The value of displacement threshold energy has not yet been agreed upon within the literature, with values ranging from 15 – 30 eV, resulting in a significant variation in σ_d and the resultant dose estimates [12,19,24,30].

During EELS experiments, the intensity of the beam was varied considerably for the acquisition of low loss and core loss spectra resulting in an inconsistent electron flux. For the acquisition of low loss spectra the beam was spread over a large area to give a low intensity (so as to avoid saturating the ccd) resulting in a near-negligible flux; when collecting the core loss however, the beam was focused over a smaller area giving a much higher intensity, comparable to the intensity during imaging. The change in fluence was accounted for by measuring the electron flux at the two acquisition intensities and recording the time spent at each; the cumulative fluence was then determined and converted to dpa.

3 Results and Discussion

3.1 TEM

Four areas of thin (<50 nm) PGA graphite were subjected to an average electron fluence of 4.2×10^{18} electrons $\text{cm}^{-2} \text{s}^{-1}$ (2.4×10^{-4} dpa s^{-1}). Images of the basal planes and electron energy loss spectra were recorded periodically throughout. The micrographs and their corresponding selected area electron diffraction (SAED) patterns shown in Figure 2 are typical of the damage produced by a 200 kV electron beam. In particular, the tortuosity (or curvature) of the (002) planes can be seen to increase, the spacing increases, and the lattice fringe length decreases. These results suggest the breakup of the graphitic structure into nanocrystalline regions with increasing dose, which in the high dose limit produce an amorphized structure. These micrographs are comparable to those obtained by Karthik and Kane [19] and Muto [31] who also investigated the effects of electron irradiation in nuclear graphite.

For comparison, Figure 2 (e) shows the effect of performing the same procedure at 400 °C. Interestingly, significantly less alteration of the atomic structure is observed, suggesting that damage is continuously annealed out at these temperatures. Further work is in progress to investigate this phenomenon in more detail. It must be noted that while these descriptions provide qualitative analysis, understanding the exact mechanisms of defect creation remains an area for investigation. A contrast change in a phase contrast TEM micrograph may not necessarily relate to a change in atomic position but may instead be due to a change in thickness or defocus. While every effort was made to ensure that images were acquired at

Scherzer defocus, awareness of the issues associated with contrast reversal is highly important when analysing these disordered structures [32].

Diffraction patterns were also recorded at regular intervals during electron beam exposure and the spacing of (002) spots were measured using intensity profiles in Digital Micrograph. Figure 3 shows an increase in plane spacing of 10% following electron irradiation of 0.31 dpa, as measured from the diffraction patterns. The arcing of the diffraction spots was also measured to assess the misalignment of layers induced during electron irradiation. To extract this information the SAED patterns were intensity normalised and the full width at half maximum (FWHM) of each diffraction arc was measured using a Graphite Anisotropy Analysis Program (GAAP) provided by A. A. Campbell at the University of Michigan [33]. GAAP measures the intensity around a ring at the (002) radius the Gaussian curves are fitted to the intensity plots and the FWHM determined. The data are presented in Figure 4 and show a 40° increase in arcing of (002) diffraction spots following 0.86 dpa of electron irradiation.

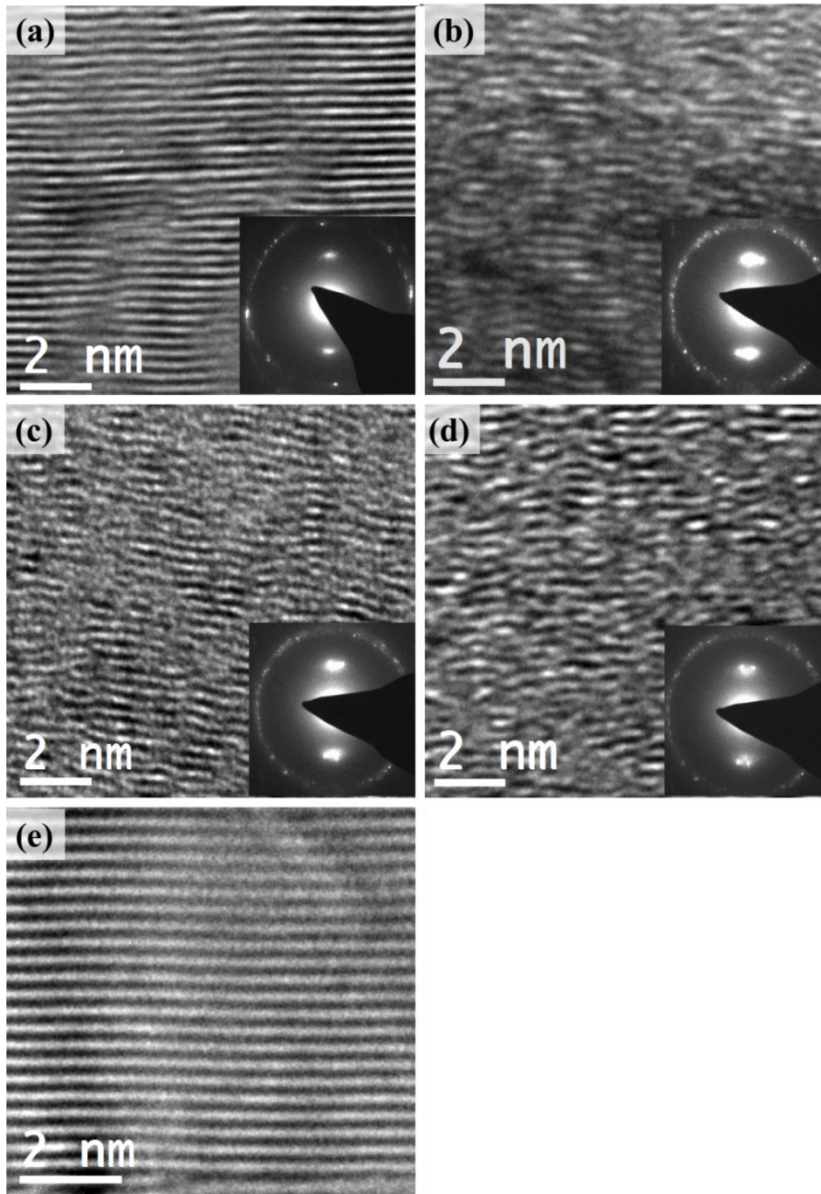


Figure 2 (a) – (d) Electron micrographs of PGA graphite with their corresponding SAED patterns during electron beam exposure at 200 keV and room temperature, receiving 4.2×10^{18} electrons $\text{cm}^{-2} \text{s}^{-1}$ (2.4×10^{-4} dpa $\text{s}^{-1} \pm 6.4\%$). (a) $D = 0.01$ dpa, (b) $D = 0.1$ dpa, (c) $D = 0.2$ dpa, (d) $D = 0.3$ dpa. (e) The same experiment was performed at 400 °C, the micrograph was recorded after a dose of 0.2 dpa.

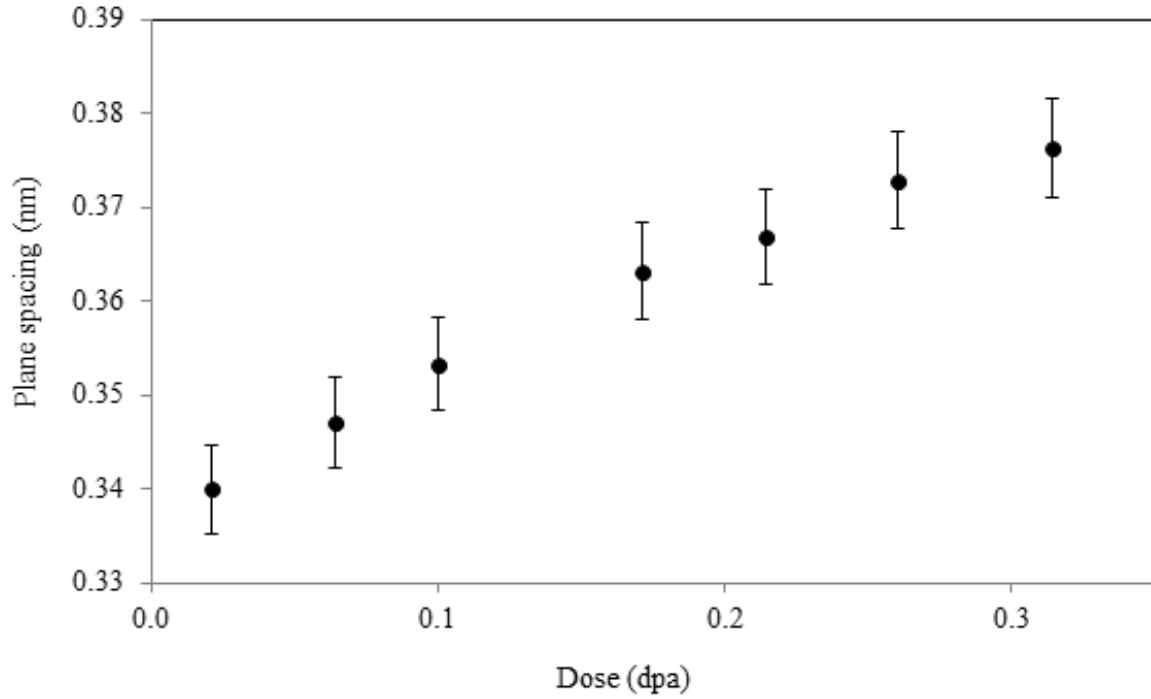


Figure 3 Change in plane spacing with respect to electron dose as measured from the spacing of (002) spot spacing in a series of SAED patterns. Error bars represent analytical error following the analysis of three damage series. Dose error = $\pm 6.4\%$

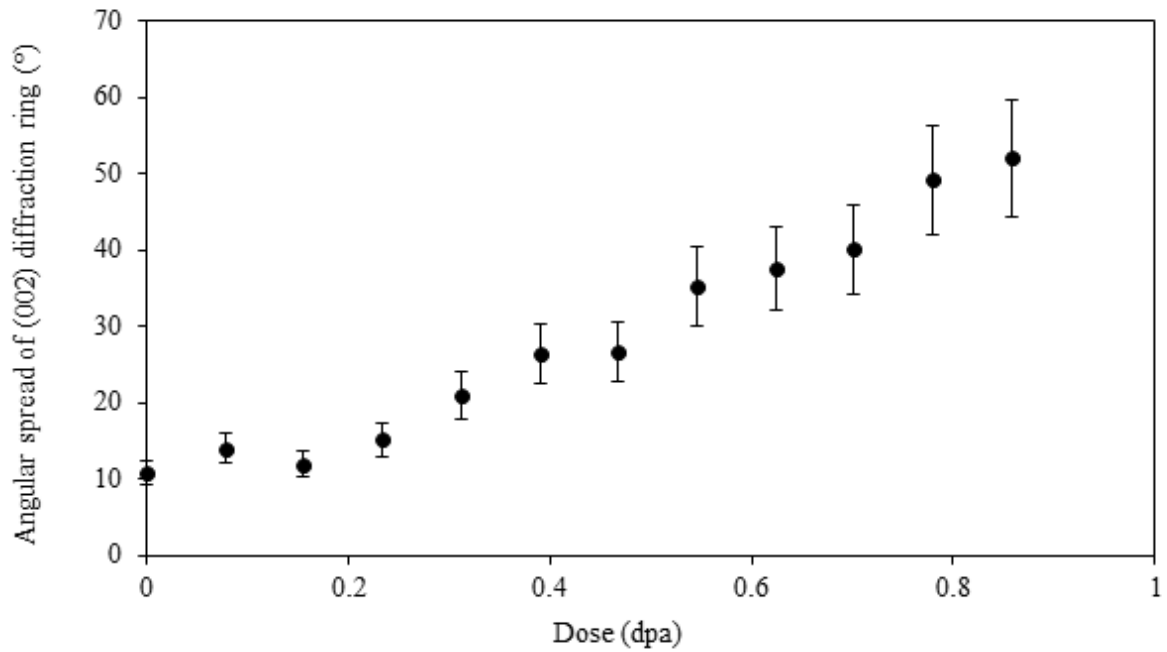


Figure 4 Change in the angular spread of the (002) spot with respect to electron dose. Data are extracted from SAED pattern analysis by measuring the FWHM of the intensity of (002) arcs. Error bars represent analytical error following the analysis of four damage series. Dose error = $\pm 6.4\%$

TEM micrographs were also analysed, using software provided by the ‘PyroMaN’ research group, to quantify the change in atomic arrangement following electron irradiation [34]. Based on analysis of (002) lattice fringes, the software provides information on fringe length, tortuosity and orientation using Fourier transform filtering and a level curve tracking algorithm [35]. Although the algorithm detects fringes even if they exceed the image boundaries, they cannot be accounted for when performing measurements since the true length and tortuosity cannot be determined. Application of the software to ordered and (electron irradiation induced) disordered areas is displayed in Figure 5 with the extracted data presented in Figure 6, 9 and 10. The lack of fringe detection (outlined in white over a filtered micrograph) for ordered structures is emphasized in Figure 5 (c) where only a third of the planes are detected. The orientation maps of these micrographs (Figure 5 (d) and (h)) show localised changes in the orientation of neighbouring planes where red indicates no relative change, yellow/green indicates a clockwise misorientation and purple/blue indicates an anticlockwise misorientation (as illustrated in the chart next to Figure 5 (h)). Statistical analysis of these orientation maps can provide additional insights into the nanostructure, including estimates of coherence lengths parallel and perpendicular to the fringes, together with the mean misorientation of the fringes at larger distances. In principle, the software is also capable of producing three dimensional models from a two dimensional electron micrograph by comparison and refinement with molecular dynamics simulations [36]. The PyroMaN image analysis technique will be applied to other structures and collaborations with the PyroMaN research group will continue in order to realise the software’s full potential.

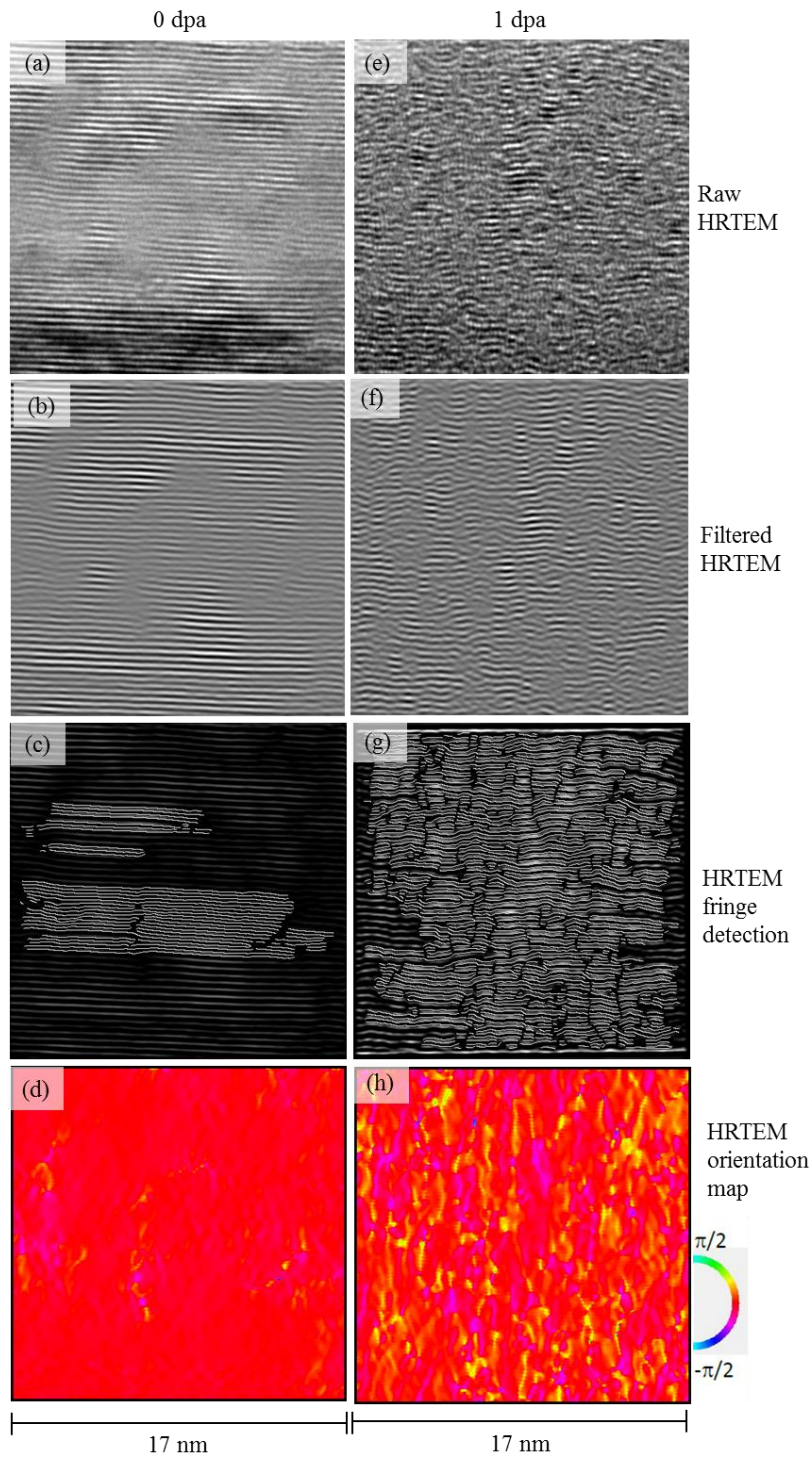


Figure 5 HRTEM images before (a-d) and after (e-h) 200 kV electron beam exposure for 5 minutes with electron flux 4.2×10^{18} electrons $\text{cm}^{-2} \text{s}^{-1}$ (2.4×10^{-4} dpa $\text{s}^{-1} \pm 6.4\%$) (equating to 1 dpa). Images (a) and (e) show the raw HRTEM images, (b) and (f) the filtered HRTEM images, (c) and (g) illustrate the detection of (002) fringes within the HTREM, and (d) and (h) are orientation maps of the original HRTEM images.

Data extracted from the fringe detection algorithm illustrated in Figure 5 (c) and (g) include fringe length (L_2) and tortuosity (τ) (the latter defined as the ratio of the total length

of a fringe to its direct end-to-end length). Figure 6, shows that for low doses where the structure is still ordered, the tortuosity of each detected fringe is relatively low, with over 75% having a tortuosity of 1 – 1.03 and a fringe length which is relatively high, extending to 8.9 nm. However when the structure becomes disordered following electron irradiation, the tortuosity increases significantly, with highs of nearly 1.14, and the (002) fringes break up into shorter lengths, 98% of which are below 1 nm in length.

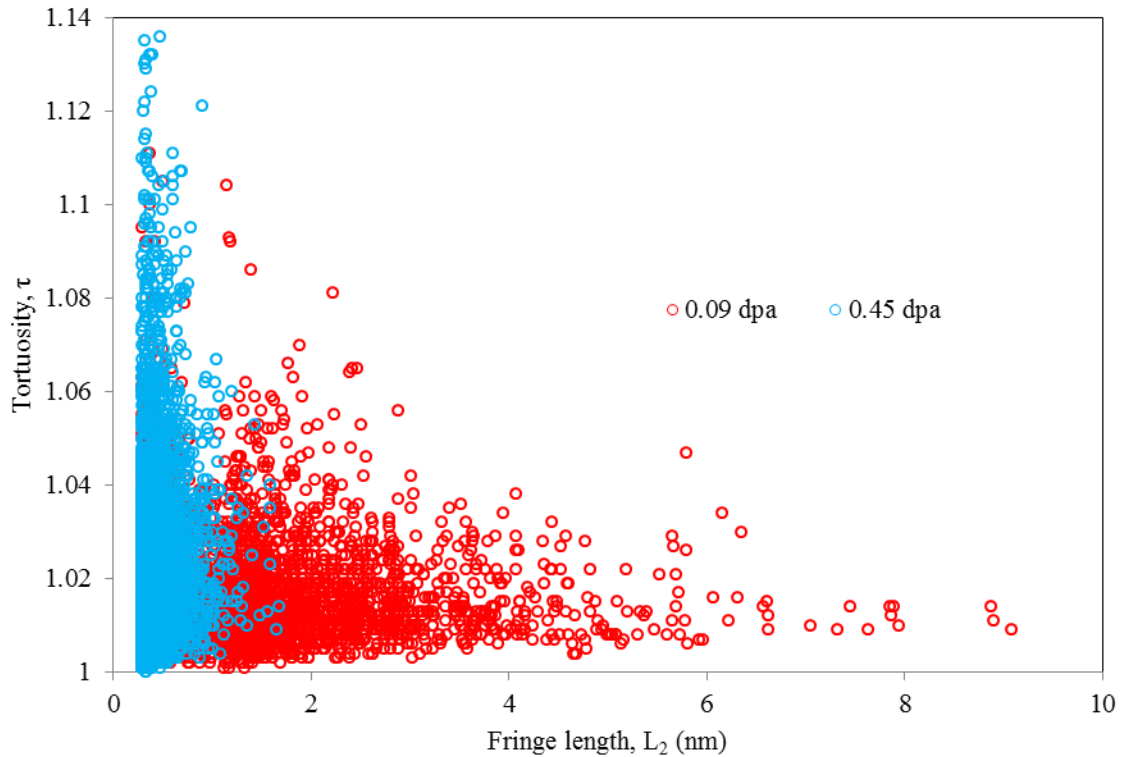


Figure 6 Comparison of fringe length and tortuosity data for the same region of interest having received low (red) and high (blue) electron irradiation doses.

A second-order (i.e. pairwise) statistical analysis of the orientation maps provides information about the relative orientation of neighbouring fringes. Referring to the schematic in Figure 7, the angles of planes to the vertical axis (ϕ_1) were measured every 0.033 nm (pixel resolution) from the origin for a set of radii (r) up to a maximum of 4 nm. Data at each angle (θ) were then plotted on a graph of mean orientation difference ($\Delta\phi$) versus distance to determine the average opening angle for the 4 nm domain as shown in Figure 7. The mean misorientation of the fringes corresponds to the plateau of the plots [37]. For example, the plot taken at 0.7 dpa plateaus at $\Delta\phi_{\max} = 8.7^\circ$ for both $\theta = 0^\circ$ and 90° (the two extremes of θ). The plateau is reached by the $\theta = 0^\circ$ data before the $\theta = 90^\circ$ data implying there is a quicker loss of orientation in the a-axis ($\theta = 0^\circ$) and domains are wider in the c-axis ($\theta = 90^\circ$). This automated procedure was performed on all micrographs acquired during electron beam

exposure to produce a series of orientation maps and a plot of orientation angle against electron dose (Figure 8). As expected it suggests that the relative orientation of planes increases with electron irradiation, but appears to plateau at high doses, suggesting there is a misorientation limit, potentially associated with the unstable transition from strained sp^2 bonding to sp^3 interlayer bonding. Although both data sets plateau at different values of $\Delta\phi$, they exhibit a similar trend suggesting there is a degree of short range homogeneity.

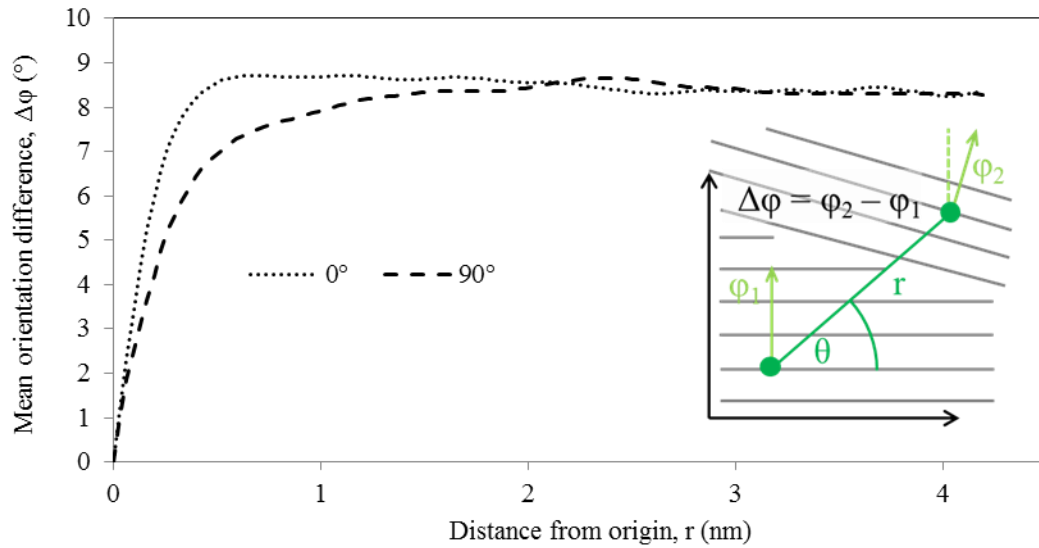


Figure 7 Change in mean orientation difference with distance from origin (r) at $\theta = 0^\circ$ and $\theta = 90^\circ$ following an electron dose of $0.7 \text{ dpa} \pm 6.4 \%$. The coherence lengths can be defined as the distance at which 90% of the value of the plateau is reached for the diagrams at 0° and 90° [37].

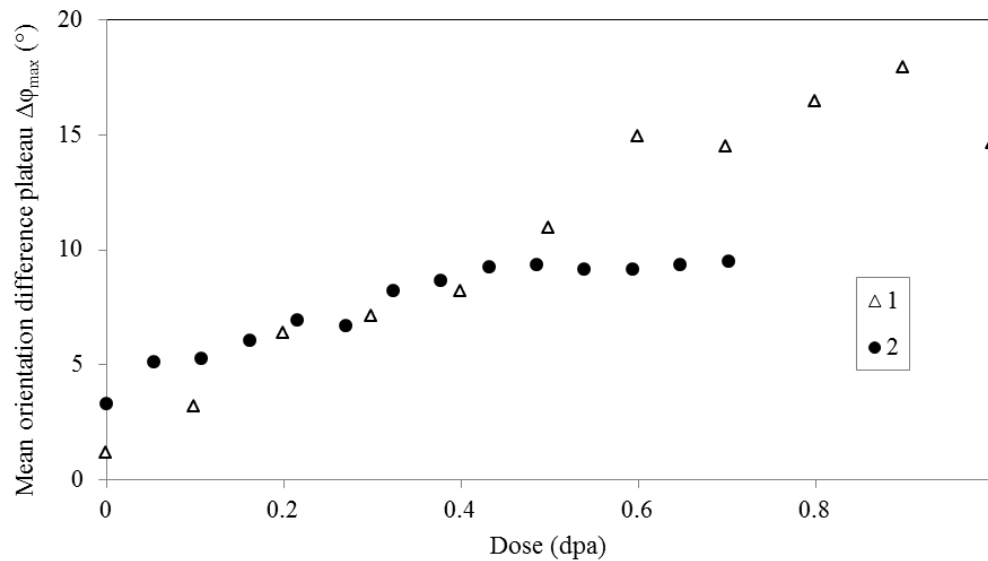


Figure 8 Change in mean orientation difference plateau, $\Delta\phi_{\text{max}}$, with electron irradiation for two irradiation data sets. Dose error = $\pm 6.4\%$

3.2 EELS

The bulk $\pi+\sigma$ valence plasmon peak in the low loss region of the spectrum was analysed; the position of the peak being determined by taking the first derivative of the spectrum. The widely agreed value for the bulk plasmon peak position of highly oriented pyrolytic graphite (HOPG) in the literature is 27 eV [38–41] (for comparison, the corresponding value for amorphous carbon is 23 eV). As illustrated in Figure 9, the plasmon peak energy for PGA graphite is consistently lower than that of HOPG. This may be due to the misorientation of the specimen's c-axis relative to the normal of the incident beam [42], in combination with the choice of the spectrometer collection angle [12,43]. During the experiments the position of the plasmon peak appears unchanged, or perhaps slightly decreases, as a function of dose to within experimental error.

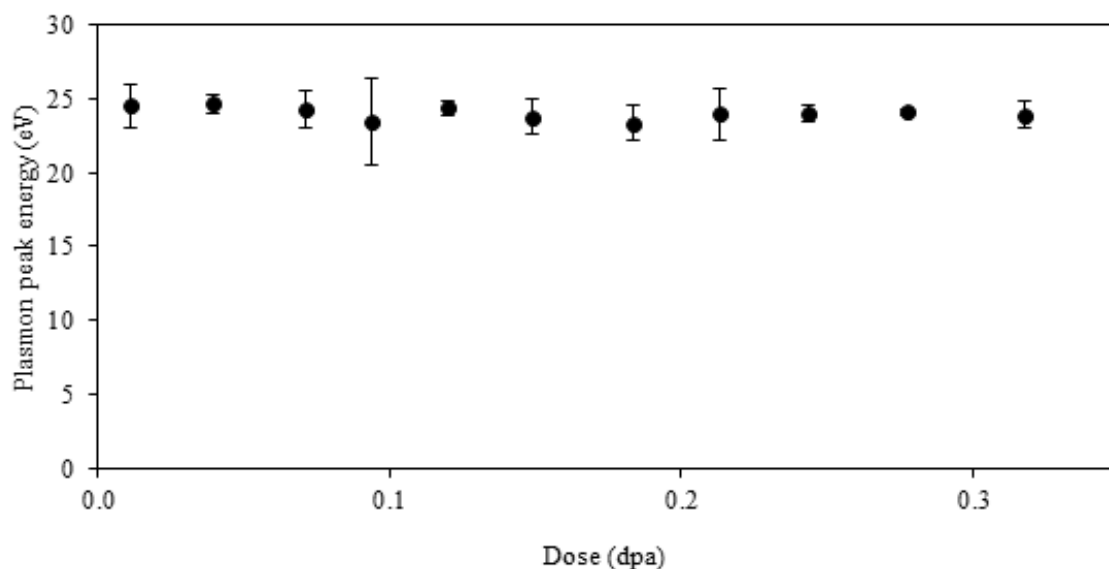


Figure 9 Change in plasmon peak position with dose. Data are averaged over two regions of electron transparent (002) oriented PGA graphite. The error bars reflect the experimental variance. Dose error = $\pm 6.4\%$

A representative set of EELS C K-edge spectra as a function of electron irradiation is presented in Figure 10 (a)-(d). The π^* peak maximum of all spectra was calibrated to 285 eV, and C K-edge spectra were acquired every 90-100 seconds along with the corresponding low loss peak which was used to deconvolute each K-edge spectra to remove plural scattering. The data extracted from the spectrum acquired at $t=0$ were used to normalise subsequent sp^2 content data. Note that even after extensive electron irradiation damage, and even though the σ^* component appears to undergo considerable change with a reduction of the graphitic order

(Figures 3-8), the presence of the π^* peak indicates that the structure retains a distinct sp^2 character.

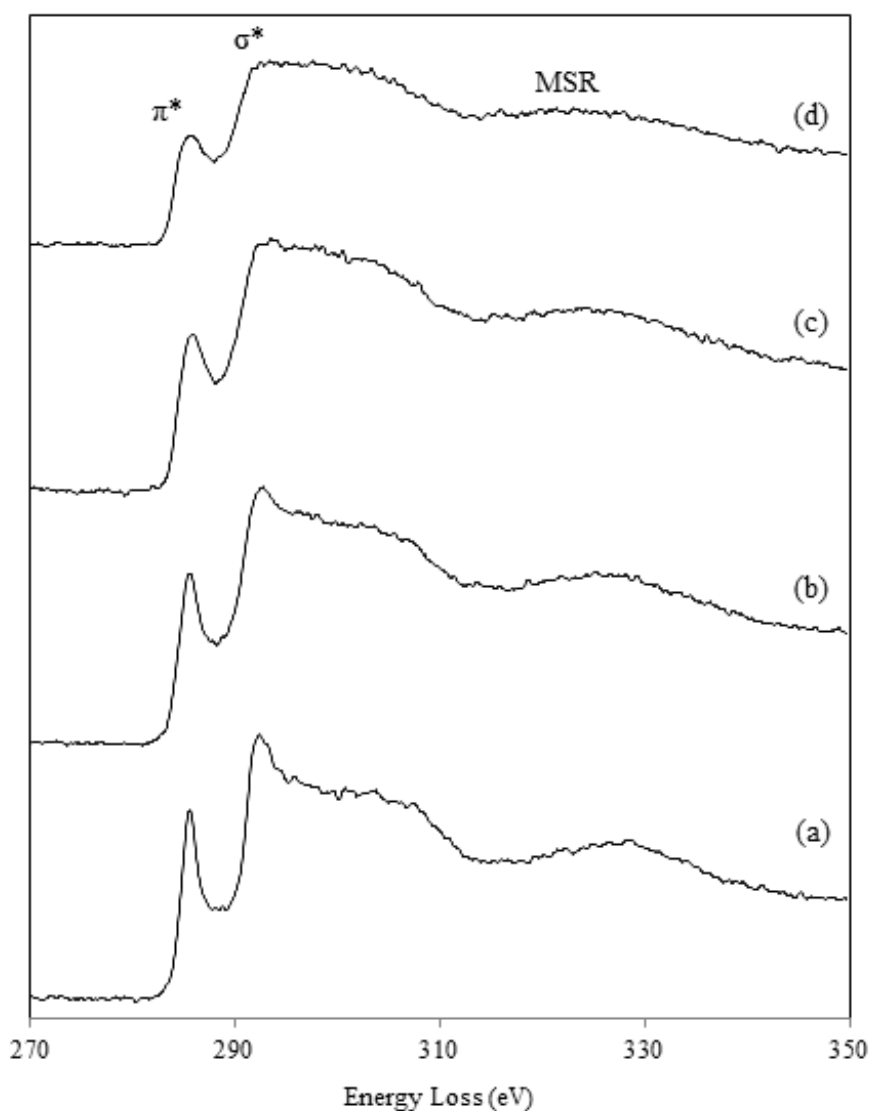


Figure 10 Change in EEL spectra with dose (D): (a) $D = 0$ dpa; (b) $D = 0.113$ dpa; (c) $D = 0.209$ dpa; (d) $D = 0.267$ dpa $\pm 6.4\%$

To characterise the ratio of (planar) sp^2 bonded carbon to total carbon, an improved automated fitting routine for the C K-edge was achieved by inclusion of two additional Gaussian curves to the method proposed by Zhang [26] which employed three Gaussian peaks (Figure 11 (a)): G1 centred at ~ 285 eV for the C=C π^* component; G2 ~ 292 eV, the C-C σ^* component and G3 ~ 300 eV, the C=C σ^* component. The additional Gaussians were positioned under the “residual” peak (~ 286 - 288 eV) described in Zhang’s method as of

uncertain origin: either from the presence of additional heterospecies (e.g. O or H) or the presence of a non-planar sp^2 -bonded (fullerene-like) carbon component, as is the case here.

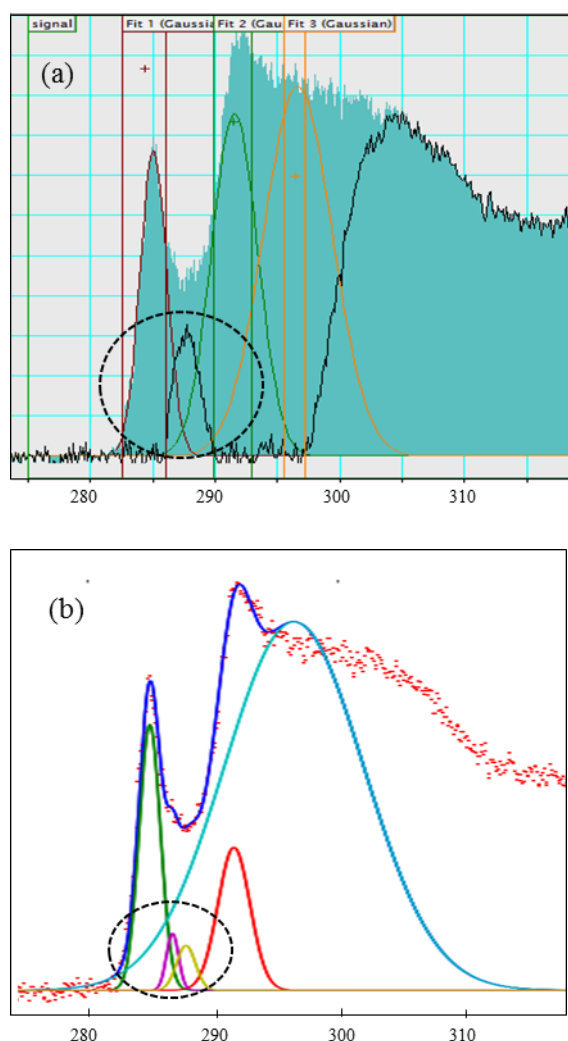


Figure 11 (a) Circled residual peak signal from a 3 Gaussian fit performed in Gatan Digital Micrograph (b) Circled residual peak signal from a 5 Gaussian fit performed in Hyperspy. The residual peak from (a) was deconvoluted into two separate peaks in (b).

All five Gaussians were fitted simultaneously using the following constraints:

- the first Gaussian (G1) centred at ~ 284.5 eV (with a constraint on the FWHM (β): $0.25 \text{ eV} \leq \beta \leq 2 \text{ eV}$);
- second Gaussian (G2) centred at ~ 291.75 eV ($2.1 \text{ eV} \leq \beta \leq 3.0 \text{ eV}$);
- third Gaussian (G3) centred at ~ 297.75 eV ($11.2 \text{ eV} \leq \beta \leq 13.1 \text{ eV}$).

While for fitting the extra two Gaussians (G4 and G5), the script fixed the FWHM and the centre of G1, G2 and G3 along with the area of G2 and G3, but allowed the area of G1 to vary in order to accommodate the new components, which were then fitted using the following constraints:

- G4 centred at ~286.5 eV ($0.2 \text{ eV} \leq \beta \leq 1.5 \text{ eV}$)
- G5 centred at ~288.5 eV ($0.2 \text{ eV} \leq \beta \leq 1.5 \text{ eV}$).

The variation of planar sp^2 content was calculated by comparing the ratio of the π^* intensity (G1) with the total C K-edge intensity (over a 20 eV window of onset 282.5 eV) which is proportional to the total number of carbon atoms present in the probed volume:

$$\text{Planar } sp^2 \text{ content} = \frac{I_{\pi^*}}{I_{\pi^*+\sigma^*}} \bigg/ \left(\frac{I_{\pi^*}}{I_{\pi^*+\sigma^*}} \right)_{t=0} \quad \text{Equation 3.1}$$

where the intensity values from the initial C K-edge spectrum were used to calculate $(I_{\pi^*} / I_{\pi^*+\sigma^*})_{t=0}$ so as to ensure all spectral changes were relative to the initial structure. As can be seen in Figure 12 the sp^2 content changed approximately linearly with respect to electron dose. The sp^2 content dropped to 76% following an exposure of 0.32 dpa, a value consistent with the typical value of 75% sp^2 carbon derived from an amorphous carbon film using this fitting method. These changes provide evidence for the introduction of atomic disorder as a result of electron beam exposure. The errors shown in Figure 12 reflect an analytical error of $\pm 6\%$ (determined by making slight changes to the energy windows to account for subjective discrepancy) and the variation in data between four separate experiments.

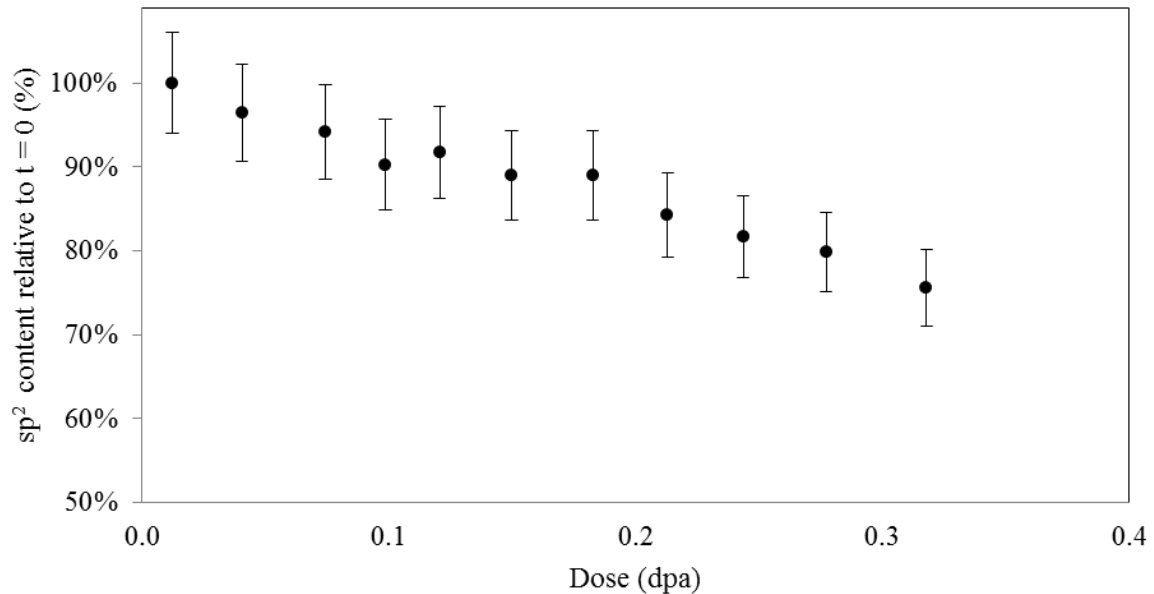


Figure 12 Change in sp^2 content with electron dose. Data were analysed using the 5 Gaussian fitting method and averaged over four regions of electron transparent (002) oriented PGA

graphite. The error bars reflect the experimental variance and analytical error. Dose error = $\pm 6.4\%$

The signals from the G4 and G5 peaks were also analysed to provide information regarding the non-planar sp^2 carbon content of the specimen by measuring the ratio between the combined intensities under G4 and G5 (I_R) and the combined intensities under the G4, G5 and G1 peaks ($I_R + sp^2$), as detailed in Equation 3.2. This ratio is proportional to the fraction of sp^2 -bonded carbon atoms which are bonded in a non-planar fashion and the increase in this quantity with increasing electron dose is plotted in Figure 13. Note the non-zero value of this quantity at zero-extrapolated dose is due to the inherent intensity in this spectral region (even in a pure planar sp^2 carbon based material) as well as any non-planar sp^2 carbon atoms located at crystallite grain boundaries within the analysed volume. Comparing the data in Figure 12 and Figure 13, it appears as though the loss of planar sp^2 bonding (very roughly a 20% decrease) is predominantly accounted for by an increase in non-planar sp^2 bonded carbon.

$$\text{Non planar } sp^2 = \frac{I_R}{I_R + sp^2} \quad \text{Equation 3.2}$$

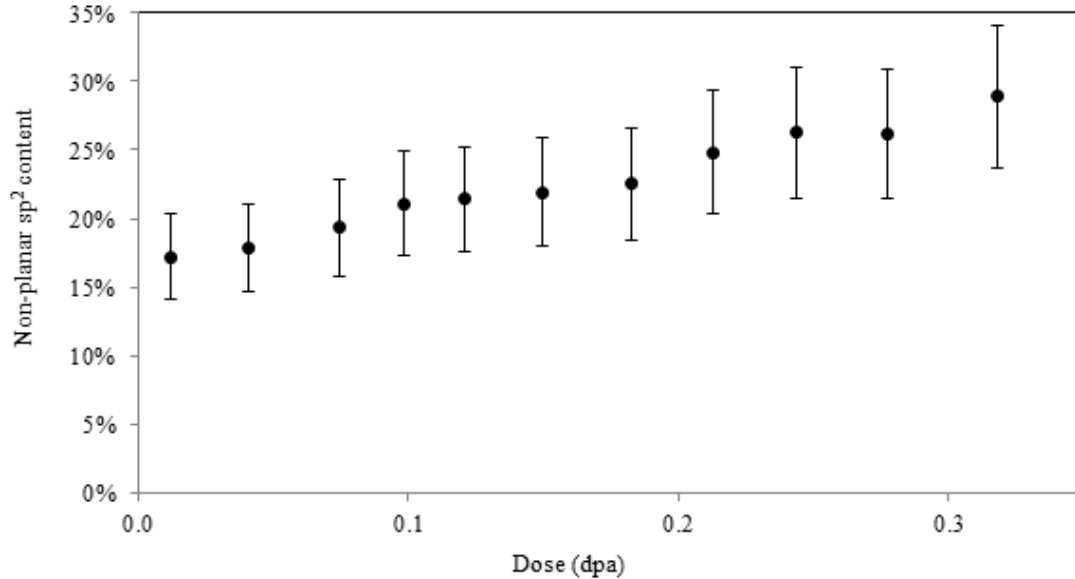


Figure 13 Change in non-planar sp^2 content with dose over two regions of electron transparent (002) oriented PGA graphite. Error bars reflect experimental variance and analytical error. Dose error = $\pm 6.4\%$

Taking the first derivative of the C K-edge spectrum to analyse the change in the MSR peak position during the electron beam damage series, we observe a slight decrease in energy relating to an increase in C-C bond length (Figure 14). The error associated with these data

increases for higher doses where the MSR peak becomes wider leading to a degree of uncertainty in peak energy assignment; the error bars in Figure 14 represent experimental variation. Results obtained by Daniels [25] following a series of graphitization experiments are analogous, whereby the graphite began as a highly disordered material with an average bond length of 1.435 Å and through annealing became a near-perfect structure with a corresponding bond length of 1.420 Å. In Daniels' case, the decrease in bond length during graphitization was attributed to a decrease in sp^3 bonding (bond length = 1.54 Å) and the removal of heteroatoms and aliphatic molecules (bond length > 1.42 Å). In the present case however, no heteroatoms and aliphatic molecules are introduced to the system and the high energy barrier between graphite and diamond phases makes sp^2 to sp^3 transformation unlikely unless at very high temperature (~1000 K) [44]. However, we have established that the electron irradiation induces nanocrystallinity with atomic disorder at crystallite grain boundaries, (Figure 2 and 7), and it is this disorder that reduces the packing efficiency of carbon atoms which is thought to increase the average bond length (e.g. for the most extreme case of amorphous carbon, the bond length increases to 1.44 Å [45]). It is thus suggested that introduction of dislocations and defects along with a bending of planes (the introduction of non-six-membered rings of carbon atoms [19]) following electron irradiation increases the average C-C bond length. One might expect that an increase in bond length would lead to a reduction in valence electron density (and thus the possible slight reduction in plasmon energy with increasing dose as shown in Figure 9).

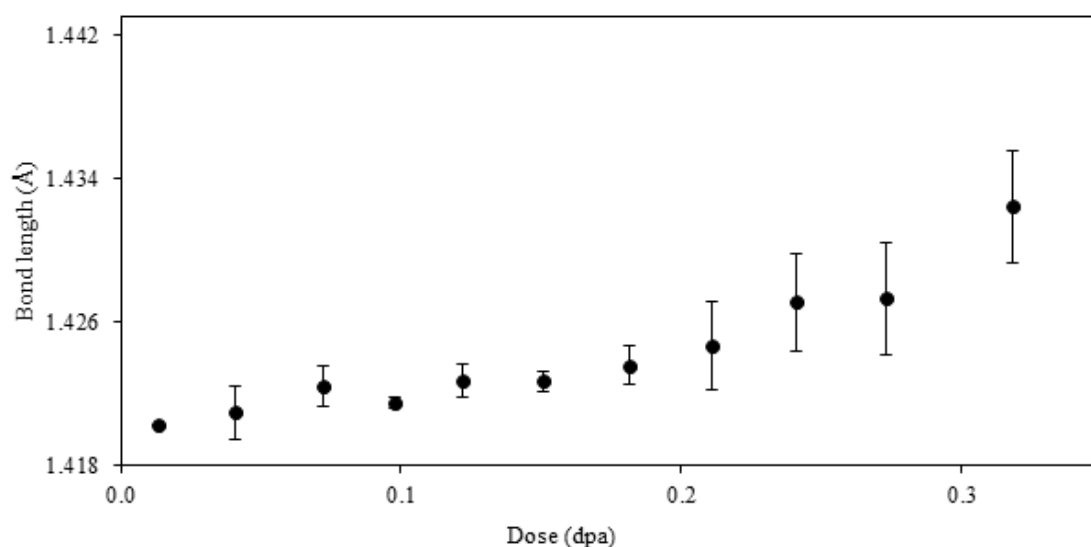


Figure 14 Change in MSR peak position with dose over two regions of electron transparent (002) oriented PGA graphite. Error bars reflect experimental variance and analytical error. Dose error = $\pm 6.4\%$

4. Final Discussion and Conclusions

We have presented a new methodology to quantitatively analyse TEM micrographs of irradiation damaged graphite. Following electron irradiation at 200 keV, a decrease in the graphite (002) fringe length and an increase in tortuosity and relative orientation was observed. Analysis of the low and core loss of several EEL spectral series indicates little or no change in valence electron density, a decrease in planar sp^2 content (to levels associated with amorphous carbon at the highest doses), an increase in non-planar sp^2 content (of inverse proportion to the planar sp^2 reduction and an increase in C-C bond length, all reflecting an increasing tortuosity of (002) layer planes and an increasing nanocrystallinity upon exposure to an increasing electron dose,

Future work will involve the application of this analysis methodology for radiation damage to electron-irradiated samples at nuclear reactor temperatures (400°C) as well as neutron-irradiated samples from nuclear reactors and materials test reactors. The full potential of the image analysis software provided by the PyroMaN research group will also be investigated.

Acknowledgements

This paper was written by Brindusa Mironov and Helen Freeman. We acknowledge Abbie Jones of the University of Manchester, UK, for the provision of polarised light micrographs and Anne. A. Campbell at the University of Michigan, U.S.A, for the provision of the Graphite Anisotropy Analysis Program (GAAP). Fred S. Hage would like to acknowledge Magnus Kristofer Nord (Norwegian University of Science and Technology, Trondheim, Norway) for assistance and useful discussions when setting up the C-K edge fitting procedure in HyperSpy (freely available from <http://hyperspy.org/>). SuperSTEM is the UK Engineering and Physical Sciences Research Council (EPSRC) National Facility for aberration-corrected STEM. Funding was provided by the National Nuclear Laboratory and EPSRC (grants EP/J502042/1 and EP/I003312/1).

References

- [1] Department of Energy & Climate Change (DECC), Table of past and present nuclear reactors in the UK, London, 2014. <https://www.gov.uk/government/policies/increasing-the-use-of-low-carbon-technologies/supporting-pages/new-nuclear-power-stations>.

- [2] R.E. Nightingale, Nuclear Graphite, Academic Press Inc., 1962.
- [3] K. Wen, J. Marrow, B. Marsden, Microcracks in nuclear graphite and highly oriented pyrolytic graphite (HOPG), *Journal of Nuclear Materials*. 381 (2008) 199–203. doi:10.1016/j.jnucmat.2008.07.012.
- [4] G.R. Hennig, Vacancies and dislocation loops in graphite, *Applied Physics Letters*. 1 (1962). doi:10.1063/1.1714334.
- [5] P.A. Thrower, W.N. Reynolds, Microstructural changes in neutron-irradiated graphite, *Journal of Nuclear Materials*. 8 (1963) 221–226. doi:10.1016/0022-3115(63)90037-0.
- [6] W. Bollmann, G.R. Hennig, Electron microscope observations of irradiated graphite single crystals, *Carbon*. 1 (1964) 525–533. doi:10.1016/0008-6223(64)90015-6.
- [7] M.I. Heggie, I. Suarez-Martinez, C. Davidson, G. Haffenden, Bukled, ruck and tuck: A proposed new model for the response of graphite to neutron irradiation, *Journal of Nuclear Materials*. 413 (2011). doi:10.1016/j.jnucmat.2011.04.015.
- [8] P.A. Thrower, R.M. Mayer, Point defects and self-diffusion in graphite, *Physica Status Solidi (a)*. 47 (1978) 11–37. doi:10.1002/pssa.2210470102.
- [9] O. Yazyev, I. Tavernelli, U. Rothlisberger, L. Helm, Early stages of radiation damage in graphite and carbon nanostructures: A first-principles molecular dynamics study, *Physical Review B*. 75 (2007) 115418. doi:10.1103/PhysRevB.75.115418.
- [10] A.A. El-Barbary, S. Trasobares, C.P. Ewels, O. Stephan, A. V Okotrub, L.G. Bulusheva, et al., Electron spectroscopy of carbon materials: experiment and theory, *Journal of Physics: Conference Series*. 26 (2006) 149–152. doi:10.1088/1742-6596/26/1/035.
- [11] J.H.W. Simmons, Radiation damage in graphite, Pergamon Press, 1965.
- [12] R.F. Egerton, Electron Energy-Loss Spectroscopy in the Electron Microscope, 3rd ed., Springer, 2011.
- [13] J. Kane, C. Karthik, D.P. Butt, W.E. Windes, R. Uvic, Microstructural characterization and pore structure analysis of nuclear graphite, *Journal of Nuclear Materials*. 415 (2011) 189–197. doi:10.1016/j.jnucmat.2011.05.053.
- [14] D.E. Baker, Graphite as a neutron moderator and reflector material, *Nuclear Engineering and Design*. 14 (1970) 413–444. doi:10.1016/0029-5493(70)90160-3.
- [15] T. Trevethan, P. Dyulgerova, C.D. Latham, M.I. Heggie, C.R. Seabourne, A.J. Scott, et al., Extended Interplanar Linking in Graphite Formed from Vacancy Aggregates, *Phys. Rev. Lett.* 111 (2013) 95501. doi:10.1103/PhysRevLett.111.095501.
- [16] P.R. Goggin, R.W. Henson, A.J. Perks, W.N. Reynolds, Dimensional changes in the irradiated graphite lattice, *Carbon*. 1 (1964) 189–200. doi:10.1016/0008-6223(64)90075-2.

- [17] R.W. Henson, J.A. Perks, J.H.W. Simmons, Lattice parameter and dimensional changes in graphite irradiated between 300 and 1350°C, *Carbon*. 6 (1968) 789–806. doi:10.1016/0008-6223(68)90065-1.
- [18] J.E. Brocklehurst, B.T. Kelly, Analysis of the dimensional changes and structural changes in polycrystalline graphite under fast neutron irradiation, *Carbon*. 31 (1992). doi:10.1016/0008-6223(93)90169-B.
- [19] C. Karthik, J. Kane, D.P.P. Butt, W.E.E. Windes, R. Uvic, In situ transmission electron microscopy of electron-beam induced damage process in nuclear grade graphite, *Journal of Nuclear Materials*. 412 (2011) 321–326. doi:10.1016/j.jnucmat.2011.03.024.
- [20] Z. Mileeva, D.K. Ross, S.M. King, A study of the porosity of nuclear graphite using small-angle neutron scattering, *Carbon*. 64 (2013) 20–26. doi:10.1016/j.carbon.2013.06.030.
- [21] S. Mrozowski, Mechanical strength, thermal expansion and structure of cokes and carbons, *Proceedings of the Conferences on Carbon*. (1954) 31.
- [22] G. Hall, B.J. Marsden, S.L. Fok, The microstructural modelling of nuclear grade graphite, *Journal of Nuclear Materials*. 353 (2006) 12–18. doi:10.1016/j.jnucmat.2006.02.082.
- [23] W. Windes, T. Burchell, R. Bratton, Graphite Technology Development Plan, 2007. <http://www.inl.gov/technicalpublications/Documents/4374056.pdf>.
- [24] F. Banhart, Irradiation effects in carbon nanostructures, *Reports on Progress in Physics*. 62 (1999) 1181–1221. doi:10.1088/0034-4885/62/8/201.
- [25] H.R. Daniels, R. Brydson, B. Rand, A.P. Brown, Investigating carbonization and graphitization using electron energy loss spectroscopy (EELS) in the transmission electron microscope (TEM), *Philosophical Magazine*. 87 (2007) 4073–4092. doi:10.1080/14786430701394041.
- [26] Z. Zhang, R. Brydson, Z. Aslam, S. Reddy, A.P. Brown, A. Westwood, et al., Investigating the structure of non-graphitising carbons using electron energy loss spectroscopy in the transmission electron microscope, *Carbon*. 49 (2011) 5049–5063. doi:10.1016/j.carbon.2011.07.023.
- [27] H. Daniels, A.P. Brown, A. Scott, T. Nichells, B. Rand, R. Brydson, Experimental and theoretical evidence for the magic angle in transmission electron energy loss spectroscopy., *Ultramicroscopy*. 96 (2003) 523–34. doi:10.1016/S0304-3991(03)00113-X.
- [28] D.B. Williams, C.B. Carter, *Transmission Electron Microscopy A textbook for Material Science*, 2nd ed., Springer, 2009.
- [29] O.S. Oen, Cross sections for atomic displacements in solids by fast electrons, ORNL-3813, Oak Ridge National Laboratory, 1965.

- [30] A. V Krashennnikov, K. Nordlund, Ion and electron irradiation-induced effects in nanostructured materials, *Journal of Applied Physics*. 107 (2010) 071301. doi:10.1063/1.3318261.
- [31] M. Takeuchi, S. Muto, T. Tanbe, Structural change in graphite under electron irradiation at low temperatures, *Journal of Nuclear Materials*. 271&272 (1999) 280–284. doi:10.1016/S0022-3115(98)00714-4.
- [32] O. Scherzer, The theoretical resolution limit of the electron microscope, *Journal of Applied Physics*. 20 (1949) 20. doi:10.1063/1.1698233.
- [33] A.A. Campbell, G.S. Was, In situ proton irradiation-induced creep at very high temperature, *Journal of Nuclear Materials*. 433 (2013) 86–94. doi:10.1016/j.jnucmat.2012.08.041.
- [34] P.I. Raynal, M. Monthieux, J.-P. Da Costa, O. Dugne, Multi-scale quantitative analysis of carbon structure and texture: III. Lattice fringe imaging analysis, in: *American Carbon Society (Ed.), Proceedings of Carbon*, Curran Associates, Inc., Clemson, South Carolina, USA., 2010: pp. 873–874.
- [35] J.-P. Da Costa, C. Germain, Level curve tracking algorithm for tectural features extraction, *Pattern Recognition*, 2000. Proceedings. 15th International Conference on. 2 (2000) 909–912. doi:10.1109/ICPR.2000.903692.
- [36] B. Farbos, P. Weisbecker, H.E. Fischer, J.-P. Da Costa, M. Lalanne, G. Chollon, et al., Nanoscale structure and texture of highly anisotropic pyrocarbons revisited with transmission electron microscopy, image processing, neutron diffraction and atomistic modeling, *Carbon*. 80 (2014) 472–489. doi:10.1016/j.carbon.2014.08.087.
- [37] J.-P. Da Costa, P. Weisbecker, B. Farbos, J.-M. Leyssale, G. Vignoles, C. Germain, Investigating carbon materials nanostructure using image orientation statistics, *Carbon*. Submitted (2014).
- [38] L. Henrard, O. Stephan, C. Colliex, Electron Energy Loss study of plasmon excitation in curved carbon network, *Synthetic Metals*. 103 (1999) 2502–2503. doi:10.1016/S0379-6779(98)01072-8.
- [39] L. Laffont, M. Monthieux, V. Serin, Plasmon as a tool for in situ evaluation of physical properties for carbon materials, *Carbon*. 40 (2002) 767–780. doi:10.1016/S0008-6223(01)00196-8.
- [40] M.H. Gass, U. Bangert, A.L. Bleloch, P. Wang, R.R. Nair, A.K. Geim, Free-standing graphene at atomic resolution, *Nature Nanotechnology*. 3 (2008) 676–81. doi:10.1038/nnano.2008.280.
- [41] R.F. Egerton, Electron energy-loss spectroscopy in the TEM, *Reports On Progress In Physics*. 72 (2009) 016502. doi:10.1088/0034-4885/72/1/016502.

- [42] A. Marinopoulos, L. Reining, V. Olevano, A. Rubio, T. Pichler, X. Liu, et al., Anisotropy and Interplane Interactions in the Dielectric Response of Graphite, *Physical Review Letters*. 89 (2002) 076402. doi:10.1103/PhysRevLett.89.076402.
- [43] R. Brydson, *Electron Energy Loss Spectroscopy*, BIOS Scientific Publishers Ltd, 2001.
- [44] F. Banhart, The role of lattice defects in the formation of new carbon structures under electron irradiation, *Japanese Society of Electron Microscopy*. 51 (2002) 189–194. doi:10.1093/jmicro/51.Supplement.S189.
- [45] M. Magnuson, M. Andersson, J. Lu, L. Hultman, U. Jansson, Electronic structure and chemical bonding of amorphous chromium carbide thin films., *Journal of Physics. Condensed Matter: An Institute of Physics Journal*. 24 (2012) 225004. doi:10.1088/0953-8984/24/22/225004.